Journal of Biomedical Optics

SPIEDigitalLibrary.org/jbo

Influence of phase function on modeled optical response of nanoparticle-labeled epithelial tissues

Can Cihan
Dizem Arifler

Influence of phase function on modeled optical response of nanoparticle-labeled epithelial tissues

Can Cihan[a] and Dizem Arifler[b]
[a]Bilkent University, Department of Electrical and Electronics Engineering, TR-06800 Bilkent, Ankara, Turkey
[b]Eastern Mediterranean University, Department of Physics, Famagusta, Cyprus

Abstract. Metal nanoparticles can be functionalized with biomolecules to selectively localize in precancerous tissues and can act as optical contrast enhancers for reflectance-based diagnosis of epithelial precancer. We carry out Monte Carlo (MC) simulations to analyze photon propagation through nanoparticle-labeled tissues and to reveal the importance of using a proper form of phase function for modeling purposes. We first employ modified phase functions generated with a weighting scheme that accounts for the relative scattering strengths of unlabeled tissue and nanoparticles. To present a comparative analysis, we repeat our MC simulations with simplified functions that only approximate the angular scattering properties of labeled tissues. The results obtained for common optical sensor geometries and biologically relevant labeling schemes indicate that the exact form of the phase function used as model input plays an important role in determining the reflectance response and approximating functions often prove inadequate in predicting the extent of contrast enhancement due to labeling. Detected reflectance intensities computed with different phase functions can differ up to ~60% and such a significant deviation may even alter the perceived contrast profile. These results need to be taken into account when developing photon propagation models to assess the diagnostic potential of nanoparticle-enhanced optical measurements.
 [DOI: 10.1117/1.3608999]

Keywords: Monte Carlo modeling; reflectance; optical sensors; nanoparticles; phase function; epithelial precancer.

Paper 11078R received Feb. 22, 2011; revised manuscript received Jun. 11, 2011; accepted for publication Jun. 16, 2011; published online Aug. 5, 2011.

1 Introduction

Naturally existing or inherent contrast between optical signals obtained from normal and precancerous tissues is due to morphological, structural, and biochemical changes associated with cancer progression.[1,2] There is currently a significant interest to develop optically active, molecular-specific contrast agents that selectively bind to cancer biomarkers in tissues and enhance intrinsic optical signals.[3–5] Metal nanoparticles can act as contrast enhancers when functionalized with biomolecules to specifically target cancer cells. These particles absorb and scatter light with distinct spectral features that can be exploited for reflectance-based diagnosis of precancer.[6–9]

Numerous computational and experimental studies have been performed to analyze the resonant optical properties of nanoparticles.[10–18] These studies describe the sensitivity of the absorption and scattering characteristics of nanoparticles to their size, shape, composition, and aggregation state as well as to the dielectric structure of the surrounding medium. Numerical results obtained with Mie theory, discrete dipole approximation, or the T-matrix approach provide an extensive insight into the resonance behavior and the relative extinction efficiency of nanospheres, nanorods, nanoshells, and even stellated nanostructures as a function of wavelength.

Characterization of the resonant response of metal nanoparticles to electromagnetic radiation in the visible and near-infrared range is a key step in understanding their potential as optical contrast agents. However, a complete assessment of the extent of achievable contrast enhancement requires a detailed analysis of photon propagation at the bulk or macroscopic tissue level. If tissues are to be labeled with nanoparticles for diagnostic purposes, the differential optical effect due to addition of these exogenous contrast enhancers needs to be quantified. Modeling studies to predict the overall reflectance profile of tissues in the presence of nanoparticles are likely to reveal the level of exogenous contrast that can be attributed to precancer development. This is particularly important for optical interrogation techniques that are based on diffuse or multiply scattered light.[19,20]

The Monte Carlo (MC) method provides a powerful computational tool to model the reflectance profile of tissues. Due to its flexibility in handling complicated tissue constructs or source-detector geometries, it has been extensively used to quantify and contrast optical signals obtained from normal and precancerous tissues.[21–24] MC modeling can also be adapted to account for the additional optical effect of external labeling and to study photon propagation in tissues labeled with metal nanoparticles. Lin et al.[25] have employed MC models to simulate how tissue reflectance changes with varying nanoshell size and concentration. Their results indicate that only a very small concentration of gold nanoshells is sufficient to alter the reflectance response of tissues. The simulations performed also demonstrate the importance of considering absorption by nanoshells even when optical extinction is dominated by scattering. It should be noted, however, that this study makes simplifying assumptions about the angular scattering properties of nanoparticle-labeled tissues; the authors argue that the anisotropy factor of tissues does not significantly change when the volume fraction of added

Address all correspondence to: Dizem Arifler, Eastern Mediterranean University, Department of Physics, Famagusta, Cyprus; Tel: (+90) 392-630-1060; Fax: (+90) 392-365-1604; E-mail: dizem.arifler@emu.edu.tr.

1083-3668/2011/16(8)/085002/12/$25.00 © 2011 SPIE

nanoparticles is small and they use the well-known Henyey-Greenstein (HG) phase function to describe the probability of scattering at different angles. From a theoretical point of view, the anisotropy factor needs to be modified in accordance with a weighting scheme that takes into account the relative scattering strengths of unlabeled tissue and nanoparticles rather than their respective volume fractions.[26] Further, although HG phase functions are frequently used to approximate the angular scattering probability distributions of tissue scatterers, they may not be sufficient to characterize the angular scattering properties of tissues labeled with nanoparticles. Nanoparticles exhibit almost isotropic scattering due to their small size and when these particles are added to highly forward scattering tissues, the resulting profile of angular scattering may no longer be represented by an HG function. A recent study by Kortun et al.[27] has shown that subtle differences in the shape of phase functions may translate into significant changes in detected reflectance intensity and the extent of these changes depends on the optical sensor geometry. Therefore, even though the approximations employed in the cited study may prove valid for the scenarios considered, a more comprehensive investigation is needed.

Another MC study reported by Kirillin et al.[28] analyzes the contrasting properties of gold nanoshells and titanium dioxide nanoparticles for optical coherence tomography imaging. The simulation results show that image contrast increases after addition of nanoparticles and the level of contrast enhancement predicted by MC simulations agrees well with experimental images. The modeling strategy described accounts for the presence of nanoparticles by defining preset probabilities of scattering by a tissue element or by an embedded nanoparticle. Scattering by a tissue element is characterized by an HG phase function, whereas the angular distribution of light scattered by a nanoparticle is computed using Mie theory. This methodology is theoretically more appropriate, but the results presented do not offer any insight into whether such a detailed approach is requisite for simulating common optical detection systems and biologically relevant labeling schemes.

The goal of the research presented in this paper is to carry out MC simulations and analyze the influence of the phase function on the modeled optical response of nanoparticle-labeled tissues. We construct normal and precancerous epithelial tissue models consisting of a thin epithelium on top of an underlying stromal layer and we consider labeling of precancerous epithelium with varying concentrations of gold nanospheres that have different sizes. Scattering in unlabeled epithelium is assumed to be characterized by an HG function and phase functions of nanospheres are calculated using Mie theory. When nanospheres are added to the epithelium, the modified phase functions can then be generated by combining these two components based on their respective scattering strengths. We employ an MC algorithm that allows random sampling of scattering directions directly from the generated functions and we compute reflectance signals at different wavelengths. The optical sensor geometries tested involve perpendicular or tilted fibers with varying source-detector separations. To present a comparative analysis, we repeat our MC simulations using HG functions with identical anisotropy factors as the modified phase functions.

Table 1 Optical properties of normal and precancerous epithelial tissue (Ref. 22).

	$\lambda = 540$ nm		$\lambda = 560$ nm		$\lambda = 600$ nm	
	Normal	Precancer	Normal	Precancer	Normal	Precancer
μ_{s1} (cm^{-1})	33.0	99.0	31.8	95.4	29.7	89.1
μ_{a1} (cm^{-1})	1.8	1.8	1.6	1.6	1.4	1.4
g_1	0.95	0.95	0.95	0.95	0.95	0.95
μ_{s2} (cm^{-1})	207.1	155.3	199.7	149.8	186.4	139.8
μ_{a2} (cm^{-1})	3.73	7.46	3.11	6.22	1.46	2.92
g_2	0.88	0.88	0.88	0.88	0.88	0.88

2 Methods

2.1 *Monte Carlo Modeling*

The fixed-weight MC code used in this study was implemented in C/C++ and has been detailed elsewhere.[22,27] Tissue layers are assumed to be infinitely wide and parallel to each other. Each layer is described by a thickness d_ℓ and several optical properties including the refractive index n_ℓ, absorption coefficient $\mu_{a\ell}$, scattering coefficient $\mu_{s\ell}$, and scattering phase function p_ℓ, where the integer subscript ℓ indicates the layer number. The phase function specifies the probability of scattering in a given direction and can be considered to represent angular distribution of scattered light during photon propagation. If the tissue layer is isotropic in terms of physical properties and there is no directional alignment of tissue components, p_ℓ depends only on the deflection angle θ.[29] The azimuthal scattering angle is generally assumed to be uniformly distributed between 0 and 2π. Our MC implementation allows simulations to be carried out with the well-known HG phase function or any phase function given in discretized form. In either case, the anisotropy factor g_ℓ is defined as the expected value of $\cos\theta$.[29]

All the simulations presented in this work were carried out with 10^8 input photons. Each simulation was repeated three times and the results shown represent averages over these three simulations. Standard errors were also computed to provide evidence for convergence of MC modeling results.

2.2 *Epithelial Tissue Parameters*

2.2.1 *Normal and precancerous tissue properties*

Epithelial tissue was modeled as a two-layer medium with $\ell = 1, 2$. The top cellular epithelium was assigned a thickness of $d_1 = 300\ \mu$m. The thickness of the stromal layer underneath the epithelium was set to a large value to mimic $d_2 = \infty$. The two tissue layers were index matched with $n_1 = n_2 = 1.35$. Table 1 lists the scattering coefficients, absorption coefficients, and the anisotropy factors of normal and precancerous tissue at three different wavelengths, namely $\lambda = 540$, 560, and 600 nm. Note that precancerous tissue is characterized by a three-fold increase in epithelial scattering, a 25% decrease in stromal scattering, and a two-fold increase in stromal absorption. These optical changes

accompany structural and morphological alterations in epithelial cell nuclei, remodeling of the stromal collagen matrix, and increased hemoglobin content in the stroma, respectively, and have been observed to provide a realistic representation of precancer development.[22] The anisotropy factors were assumed to be wavelength independent with $g_1 = 0.95$ and $g_2 = 0.88$ for both normal and precancerous tissue. The HG phase function was used to describe the angular scattering probability distributions in the epithelial and stromal layers. This is an analytical function that specifies the probability that a photon is scattered in the angular interval $(\theta, \theta + d\theta)$ and is expressed as[27,29]

$$p_\ell(\theta) = \frac{1 - g_\ell^2}{2(1 + g_\ell^2 - 2g_\ell \cos\theta)^{3/2}} \sin\theta, \tag{1}$$

such that

$$\int_0^\pi p_\ell(\theta) d\theta = 1. \tag{2}$$

2.2.2 *Nanoparticle-labeled precancerous tissue properties*

We assume that when metal nanoparticles are added to tissue, they will selectively attach to cancer cells and will eventually be distributed throughout the precancerous epithelium. This is a simple and yet realistic approximation since nanoparticles can be functionalized to specifically bind to cellular biomarkers that are overexpressed in epithelial precancers.[3–9,15,16,18] While the stromal optical properties remain unchanged, the scattering and absorption properties of precancerous epithelium need to be modified to account for the additional optical effect of these particles. Let μ_s^{np} and μ_a^{np} be the differential scattering and absorption coefficients due to the addition of nanoparticles, respectively. Under the assumption of independent scattering, these coefficients can be calculated as[25]

$$\mu_s^{np} = C_{sca} \frac{f}{V}; \quad \mu_a^{np} = C_{abs} \frac{f}{V}, \tag{3}$$

where C_{sca} and C_{abs} are the scattering and absorption cross sections of nanoparticles, f is the volume fraction of nanoparticles added to the epithelial layer, and V is the volume occupied by a single nanoparticle. The modified scattering and absorption coefficients are then given by

$$\mu_{s1}^* = \mu_{s1} + \mu_s^{np}; \quad \mu_{a1}^* = \mu_{a1} + \mu_a^{np}. \tag{4}$$

The modified phase function can be calculated by adopting a weighting scheme that accounts for the relative scattering strengths of unlabeled epithelium and nanoparticles. If the phase function of nanoparticles is denoted by p^{np}, the modified phase function of the epithelial layer can be computed as[26]

$$p_1^* = \frac{\mu_{s1} p_1 + \mu_s^{np} p^{np}}{\mu_{s1}^*}. \tag{5}$$

Note that the anisotropy factor of the nanoparticle-labeled epithelium is given by

$$g_1^* = \frac{\mu_{s1} g_1 + \mu_s^{np} g^{np}}{\mu_{s1}^*}, \tag{6}$$

where g^{np} is the anisotropy factor of nanoparticles.

In this study, we considered nanoparticles in the form of gold nanospheres with diameters of 40, 80, and 120 nm. The values of the complex dielectric function for gold were obtained from experimental data reported by Johnson and Christy.[30] These values were then corrected for intrinsic size effects as described by Averitt et al.,[31] Link and El-Sayed,[32] and Berciaud et al.[33] Although the corrections were minimal even for 40-nm nanospheres, it was necessary to incorporate intrinsic size effects for generality and completeness. Since nanospheres were to be added to the epithelial layer, they were assumed to be embedded in a medium with a refractive index of $n_1 = 1.35$ and their optical properties were computed using Mie theory for homogeneous spherical scatterers.[34] Mie theory calculations were performed for optical wavelengths in increments of 20 nm and the results showed that 40-, 80-, and 120-nm nanospheres had maximum scattering cross sections at $\lambda = 540$, 560, and 600 nm, respectively. The influence of phase function on modeled optical response of nanoparticle-labeled tissues is likely to be most pronounced where nanoparticles exhibit strong scattering. Hence, these three representative wavelengths were selected for MC simulations presented in this paper.

Three different volume fractions were tested to assess the effect of particle concentration on epithelial optical properties. These volume fractions were $f_1 = 0.0005\%$, $f_2 = 0.001\%$, and $f_3 = 0.005\%$. Note that the percentages given correspond to about 1.5×10^{11} to 1.5×10^{12} particles/mL for 40-nm nanospheres, 1.9×10^{10} to 1.9×10^{11} particles/mL for 80-nm nanospheres, and 5.5×10^{9} to 5.5×10^{10} particles/mL for 120-nm nanospheres, and are comparable to concentration ranges reported in previous experimental and computational studies.[7,15,18,20,25,28,35] At such low concentrations, the assumption of independent scattering is justifiable and the modified optical properties can be calculated according to Eqs. (3)–(6).

It is important to note that since Mie theory can only be used to compute the intensity of scattered light at discrete angles, care must be taken to ensure proper normalization of modified phase functions given by Eq. (5). Assume that the intensity of light scattered by nanospheres is denoted by $I(\theta)$, where $\theta \in \{0, 1, \ldots, 180\}$ is the scattering angle in degrees. The scattering phase function p^{np} is then calculated as

$$p^{np}(\theta) = \frac{I(\theta) \sin\theta \Delta\theta}{\sum_{\theta=0}^{180} I(\theta) \sin\theta \Delta\theta}. \tag{7}$$

The angular interval $\Delta\theta$ equals 1 and cancels out in Eq. (7), but it has been included for completeness. Similarly, a discretized version of Eq. (1) can be used to express p_1 for $\theta \in \{0, 1, \ldots, 180\}$. The modified phase function p_1^* will then be defined only for discrete directions, but continuous scattering angles can still be obtained via a random-variate generation algorithm applied in conjunction with an interpolation scheme.[27]

Simulations for nanoparticle-labeled precancerous tissue were carried out with modified epithelial phase functions computed using Eq. (5). These simulations were then repeated with g_1^*-equivalent HG functions to present a comparative analysis.

2.3 *Optical Sensor Parameters*

It is well established that the probing depth of a given source-detector fiber pair depends on the separation and angular orientation of the fibers.[22,36] Optical sensor geometries that preferentially probe the top epithelial layer are expected to demonstrate a greater degree of sensitivity to the form of the phase function

Table 2 Modified optical properties of precancerous epithelium labeled with 40-, 80-, and 120-nm gold nanospheres. Three different volume fractions are considered: $f_1 = 0.0005\%$, $f_2 = 0.001\%$, and $f_3 = 0.005\%$.

	$\lambda = 540$ nm			$\lambda = 560$ nm			$\lambda = 600$ nm		
	f_1	f_2	f_3	f_1	f_2	f_3	f_1	f_2	f_3
40 nm									
μ_{s1}^* (cm^{-1})	99.4	99.8	103.2	95.7	96.0	98.6	89.2	89.4	90.5
μ_{a1}^* (cm^{-1})	6.5	11.3	49.3	4.2	6.8	27.7	2.1	2.7	7.9
g_1^*	0.95	0.94	0.91	0.95	0.94	0.92	0.95	0.95	0.94
80 nm									
μ_{s1}^* (cm^{-1})	101.3	103.5	121.6	98.3	101.3	124.7	90.9	92.7	107.2
μ_{a1}^* (cm^{-1})	5.3	8.8	36.8	4.8	7.9	33.1	2.5	3.6	12.2
g_1^*	0.93	0.91	0.78	0.92	0.90	0.73	0.93	0.91	0.79
120 nm									
μ_{s1}^* (cm^{-1})	100.8	102.7	117.3	97.9	100.4	120.3	92.5	95.8	122.7
μ_{a1}^* (cm^{-1})	3.0	4.2	13.7	2.6	3.6	11.8	2.1	2.8	8.4
g_1^*	0.93	0.92	0.81	0.93	0.90	0.76	0.92	0.88	0.69

used for nanoparticle-labeled precancerous epithelium. In order to assess the extent of geometry-dependent influence of epithelial phase function on detected reflectance, we modeled two fiber optic probe configurations that are commonly employed for optical measurements. Both configurations consisted of a single source fiber and multiple detector fibers positioned at different distances from the source. The fibers were all in contact with the tissue surface and they were assigned a diameter of 100 μm and a numerical aperture of 0.11 (in air). The refractive indices of the fibers were set to 1.5 and the material between the fibers was index matched to the epithelial layer to mimic a highly absorptive interface. In the first configuration, the source and detector fibers were perpendicular to the tissue surface. In the second configuration, the fibers were oriented such that the distal ends of a given source-detector fiber pair were tilted toward each other. Each fiber made an angle of 30 deg with respect to the tissue normal, but the fiber tips remained parallel to the tissue surface. For the two configurations described, we present and discuss results for center-to-center source-detector separations of 150 and 300 μm.

3 Results

3.1 *Modified Optical Properties of Nanoparticle-Labeled Precancerous Epithelium*

Table 2 lists the modified optical properties of precancerous epithelium labeled with 40-, 80-, and 120-nm nanospheres. The results show that the scattering and absorption coefficients can significantly change when nanoparticles are added to the epithelial layer. As expected, the extent of these changes depends on the size and concentration of the nanoparticles as well as the wavelength. The largest incremental increase in the epithelial scattering coefficient occurs at $\lambda = 540$, 560, and 600 nm for 40-, 80-, and 120-nm nanospheres, respectively. The most significant increase in the epithelial absorption coefficient, on the other hand, is observed at $\lambda = 540$ nm for all nanospheres. It is also evident that the addition of nanoparticles can lead to a substantial decrease in the anisotropy factor and this appears to be most pronounced at wavelengths corresponding to respective scattering cross section maxima. Overall, modifications for the absorption coefficient are more extensive when small nanospheres are added, whereas larger nanospheres tend to produce more significant changes in the scattering coefficient and the anisotropy factor.

Figures 1–3 provide representative examples to illustrate how the phase function of precancerous epithelium changes due to the addition of nanoparticles. Figure 1 presents the results obtained at $\lambda = 540$ nm for varying concentrations of 40-nm nanospheres. Each plot shows the HG phase function characterizing unlabeled epithelium, the Mie phase function of a single 40-nm nanosphere, the modified phase function calculated using Eq. (5), and an HG phase function with an identical anisotropy factor as the modified phase function. For all of the plots presented, the angular resolution for the scattering angle is 1 deg. Note that the probability of scattering at 0 and 180 deg is zero due to the inclusion of the $\sin\theta$ factor in Eqs. (1) and (7), and these data points have been excluded from the semilog plots. For $f_1 = 0.0005\%$ [Fig. 1(a)], the addition of 40-nm nanospheres does not affect the epithelial phase function over the angular range ~0 to 90 deg, but there is a slight increase in scattering probability for larger angles; the g_1^*-equivalent

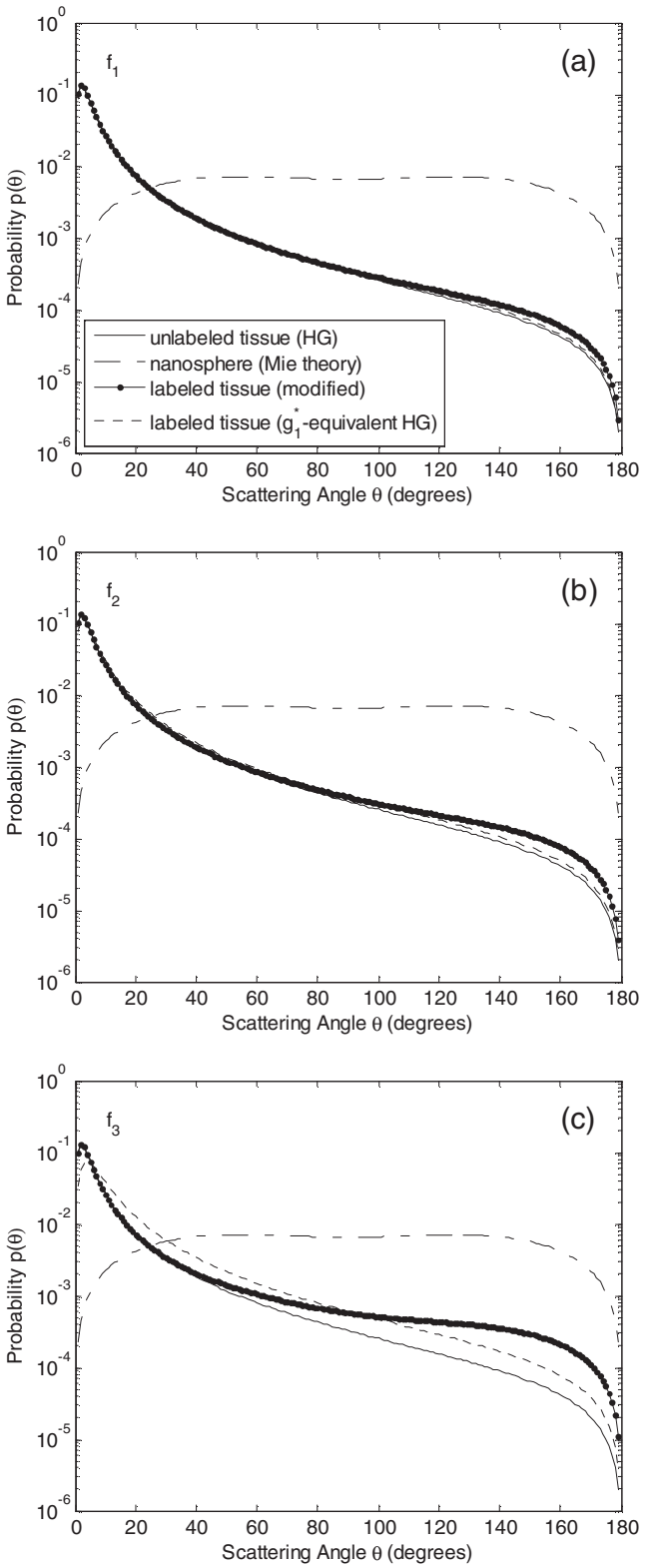

Fig. 1 Modified phase functions of precancerous epithelium labeled with 40-nm gold nanospheres and their g_1^*-equivalent HG counterparts for $\lambda = 540$ nm. The HG function characterizing unlabeled precancerous epithelium ($g_1 = 0.95$) and the Mie phase function of a single 40-nm nanosphere ($g^{np} = 0.0016$) are also shown. Three different volume fractions are considered: (a) $f_1 = 0.0005\%$; $g_1^* = 0.95$, (b) $f_2 = 0.001\%$; $g_1^* = 0.94$, and (c) $f_3 = 0.005\%$; $g_1^* = 0.91$.

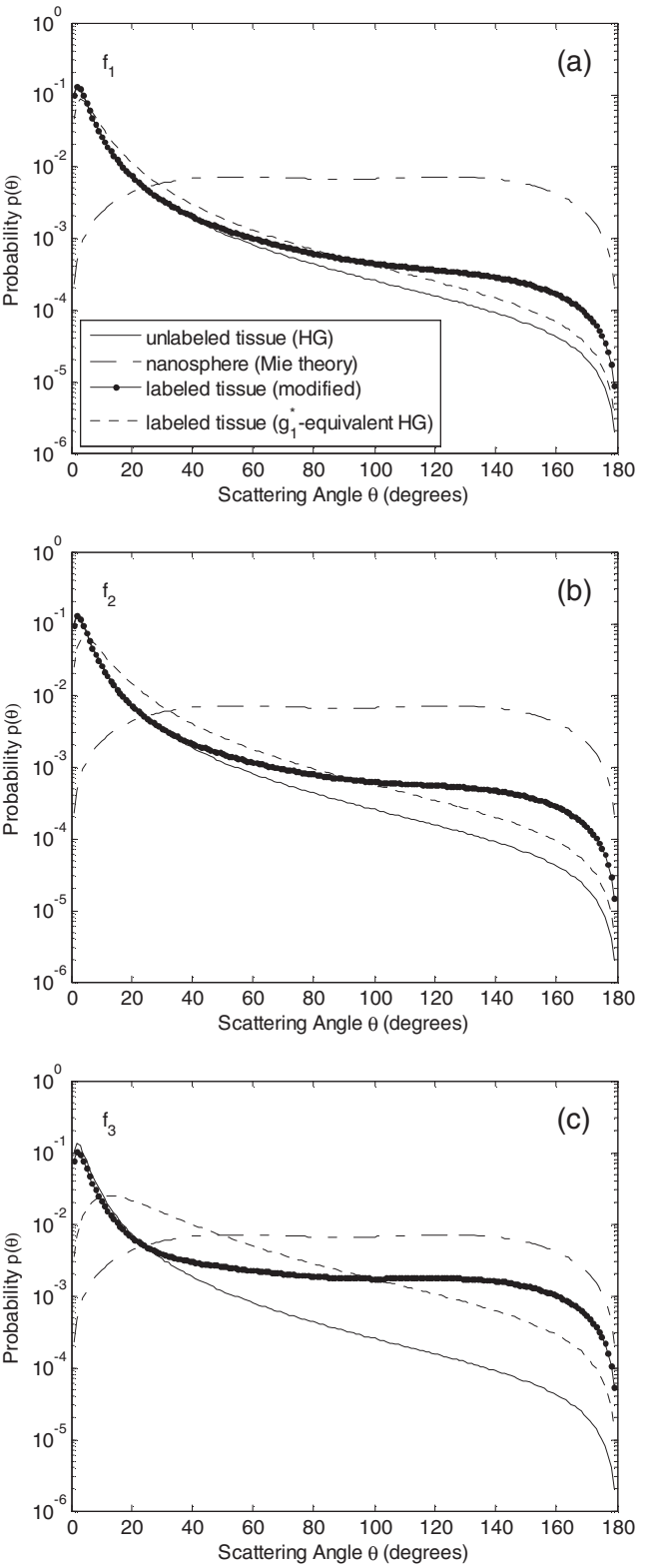

Fig. 2 Modified phase functions of precancerous epithelium labeled with 80-nm gold nanospheres and their g_1^*-equivalent HG counterparts for $\lambda = 560$ nm. The HG function characterizing unlabeled precancerous epithelium ($g_1 = 0.95$) and the Mie phase function of a single 80-nm nanosphere ($g^{np} = 0.0049$) are also shown. Three different volume fractions are considered: (a) $f_1 = 0.0005\%$; $g_1^* = 0.92$, (b) $f_2 = 0.001\%$; $g_1^* = 0.90$, and (c) $f_3 = 0.005\%$; $g_1^* = 0.73$.

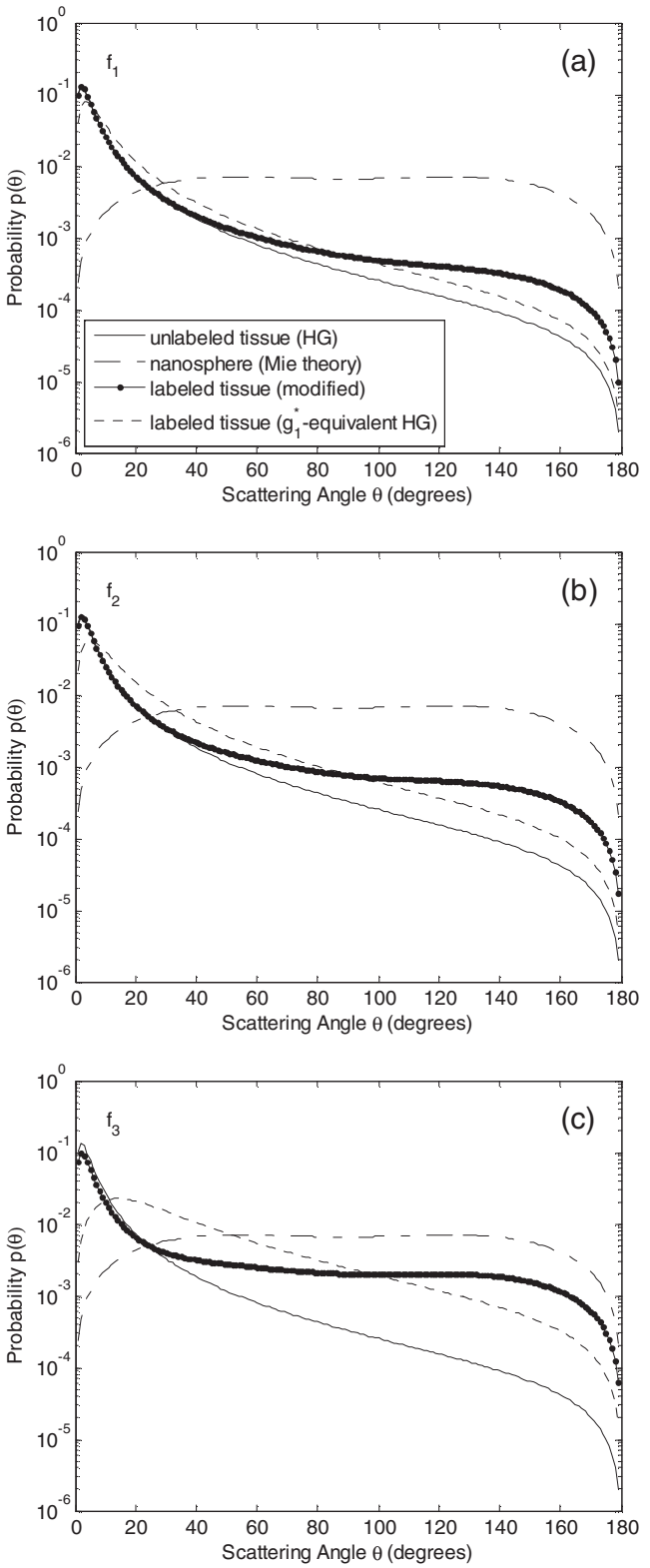

Fig. 3 Modified phase functions of precancerous epithelium labeled with 120-nm gold nanospheres and their g_1^*-equivalent HG counterparts for $\lambda = 600$ nm. The HG function characterizing unlabeled precancerous epithelium ($g_1 = 0.95$) and the Mie phase function of a single 120-nm nanosphere ($g^{np} = 0.0067$) are also shown. Three different volume fractions are considered: (a) $f_1 = 0.0005\%$; $g_1^* = 0.92$, (b) $f_2 = 0.001\%$; $g_1^* = 0.88$, and (c) $f_3 = 0.005\%$; $g_1^* = 0.69$.

HG function falls short of predicting this high-angle scattering enhancement. The results for $f_2 = 0.001\%$ [Fig. 1(b)] show similar trends, but there are larger differences between the modified phase function and its g_1^*-equivalent HG counterpart. For $f_3 = 0.005\%$ [Fig. 1(c)], the addition of 40-nm nanospheres leads to a significant increase in scattering probability for angles $>\sim$30 deg; with the g_1^*-equivalent HG phase function, the scattering probability is underestimated for $<\sim$10 deg, overestimated over the angular range $\sim$10 to 90 deg, and underestimated again for $>\sim$90 deg.

Similarly, Fig. 2 shows the modified phase functions obtained at $\lambda = 560$ nm for varying concentrations of 80-nm nanospheres. Progressively increasing levels of high-angle scattering enhancement are observed for $f_1 = 0.0005\%$ [Fig. 2(a)], $f_2 = 0.001\%$ [Fig. 2(b)], and $f_3 = 0.005\%$ [Fig. 2(c)]. In addition to a significant increase in high-angle scattering probability, the modified phase function for $f_3 = 0.005\%$ is also characterized by a discernible drop in scattering probability for angles $<\sim$30 deg. With the respective g_1^*-equivalent HG phase functions, the scattering probability is underestimated for $<\sim$10 deg, overestimated over the angular range $\sim$10 to 90 deg, and underestimated again for $>\sim$90 deg; the extent of these deviations increases with increasing volume fraction.

Finally, Fig. 3 presents the results obtained at $\lambda = 600$ nm for varying concentrations of 120-nm nanospheres. The modified phase functions are similar to those shown in Fig. 2 for 80-nm nanospheres, but the level of high-angle scattering enhancement is considerably higher. It is also apparent that the differences between the modified phase functions and their g_1^*-equivalent HG counterparts are more extensive for 120-nm nanospheres.

3.2 *Influence of Phase Function on Modeled Reflectance*

Figures 4–7 show the modeled reflectance response for different source-detector geometries simulated. For each labeling scheme considered, the simulation results for normal and unlabeled precancerous tissue are plotted along with the results for labeled precancerous tissue in order to enable a relative assessment of intensity differences. Note that the reflectance values in each figure have been scaled such that the intensity at $\lambda = 600$ nm equals one for normal tissue. In all cases, the error bars corresponding to standard error values computed over three simulations are the same size as or smaller than the symbols shown. The dashed lines connecting the data points for modified and g_1^*-equivalent HG phase functions are meant to guide the eye and highlight the influence of phase function on the reflectance profile of labeled precancerous tissue.

The results presented in Fig. 4 demonstrate that when the fibers are oriented perpendicular to the tissue surface and are separated by a distance of 150 μm, the reflectance intensity of unlabeled precancerous tissue is lower compared to that of normal tissue. The addition of 40-nm nanospheres enhances this negative contrast by causing a further reduction in detected reflectance intensity and it is evident that the form of the phase function used does not have any influence on simulation output [Figs. 4(a)–4(c)]. Similar trends are observed for 80-nm nanospheres added at low concentrations [Figs. 4(d)–4(e)], but the results are sensitive to the form of the phase function used

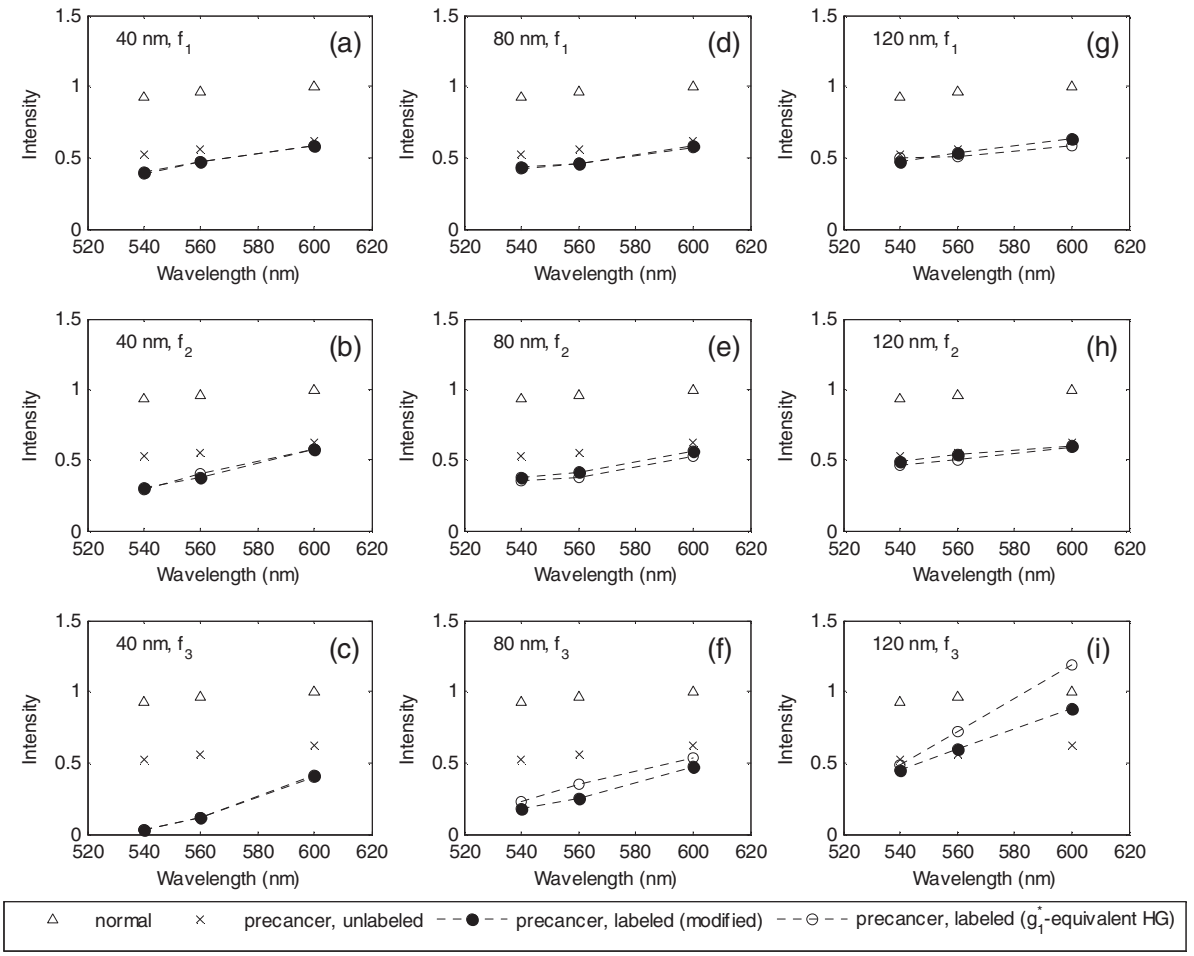

Fig. 4 Modeled reflectance response of normal tissue, unlabeled precancerous tissue, and precancerous tissue labeled with gold nanospheres. Possible combinations of nanosphere sizes (40, 80, and 120 nm) and volume fractions ($f_1 = 0.0005\%$, $f_2 = 0.001\%$, and $f_3 = 0.005\%$) result in nine different labeling schemes: (a) 40 nm; f_1, (b) 40 nm; f_2, (c) 40 nm; f_3, (d) 80 nm; f_1, (e) 80 nm; f_2, (f) 80 nm; f_3, (g) 120 nm; f_1, (h) 120 nm; f_2, and (i) 120 nm; f_3. The source and detector fibers are oriented perpendicular to the tissue surface and are separated by a center-to-center distance of 150 μm.

when the volume fraction is high; the most significant difference appears at $\lambda = 560$ nm, where the intensity obtained with the HG phase function is ~40% higher than that obtained with the modified phase function [Fig. 4(f)]. Interestingly, the addition of 120-nm nanospheres at low concentrations does not lead to any contrast enhancement [Figs. 4(g)–4(h)]. For the highest volume fraction tested, however, the use of different phase functions can give rise to considerable intensity variations; most notably, the intensity obtained with the modified phase function at $\lambda = 600$ nm suggests a reduction of negative signal contrast, whereas the intensity obtained with the HG phase function is ~35% higher and points to a positive contrast relative to normal tissue [Fig. 4(i)].

Figure 5 shows the reflectance response for perpendicular source and detector fibers separated by a center-to-center distance of 300 μm. The basic trends are similar to those presented in Fig. 4 for a source-detector separation of 150 μm, but differences between the simulation results for modified and HG phase functions are more significant when 120-nm nanospheres are added at the highest volume fraction shown; for instance, the intensities obtained with HG phase functions are ~60% higher at $\lambda = 560$ and 600 nm and this alters the perceived contrast profile [Fig. 5(i)].

The results corresponding to tilted fibers with a center-to-center source-detector separation of 150 μm are shown in Fig. 6. Note that the vertical scale for each subplot has been adjusted so that intensity differences due to labeling can be clearly identified. When the fibers are tilted with respect to the tissue surface, the reflectance intensity of unlabeled precancerous tissue is higher compared to that of normal tissue and, hence, the inherent diagnostic contrast is positive. It appears that this source-detector geometry is highly sensitive to the form of the phase function used to simulate labeled tissue; considerable differences arise for all of the labeling schemes considered. Particularly for 80- and 120-nm nanospheres, both forms of phase function point to an increase in detected reflectance intensity relative to unlabeled tissue, but positive contrast enhancement predicted with modified phase functions is consistently higher than that predicted with their g_1^*-equivalent HG counterparts. The largest differences (~35%) occur at $\lambda = 560$ nm when 80-nm nanospheres are added at a volume fraction of $f_2 = 0.001\%$ [Fig. 6(e)] and at $\lambda = 600$ nm when 120-nm nanospheres are added at a volume fraction of $f_1 = 0.0005\%$ [Fig. 6(g)].

Figure 7 depicts the modeled reflectance response when the separation between tilted source and detector fibers is increased

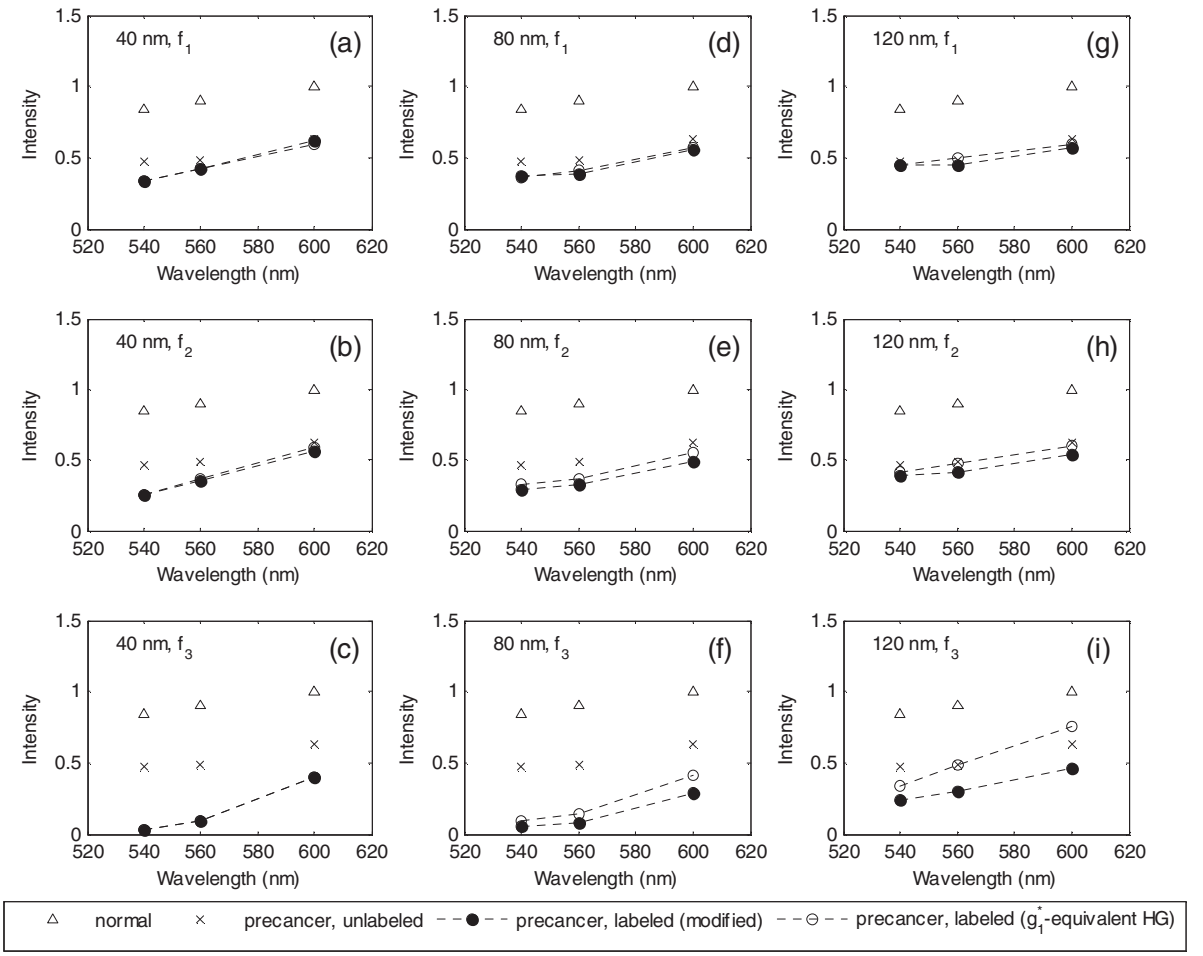

Fig. 5 Modeled reflectance response of normal tissue, unlabeled precancerous tissue, and precancerous tissue labeled with gold nanospheres. Possible combinations of nanosphere sizes (40, 80, and 120 nm) and volume fractions ($f_1 = 0.0005\%$, $f_2 = 0.001\%$, and $f_3 = 0.005\%$) result in nine different labeling schemes: (a) 40 nm; f_1, (b) 40 nm; f_2, (c) 40 nm; f_3, (d) 80 nm; f_1, (e) 80 nm; f_2, (f) 80 nm; f_3, (g) 120 nm; f_1, (h) 120 nm; f_2, and (i) 120 nm; f_3. The source and detector fibers are oriented perpendicular to the tissue surface and are separated by a center-to-center distance of 300 μm.

to 300 μm. Note again that the vertical scales have been adjusted to maintain clarity of the plots. These results further illustrate that intensity changes predicted with different forms of phase function can appreciably vary, especially for larger nanospheres. As in Fig. 6, the largest relative differences ($\sim$25%) occur at $\lambda = 560$ nm when 80-nm nanospheres are added at a volume fraction of $f_2 = 0.001\%$ [Fig. 7(e)] and at $\lambda = 600$ nm when 120-nm nanospheres are added at a volume fraction of $f_1 = 0.0005\%$ [Fig. 7(g)].

As a supplementary summary of the main trends observed in Figs. 4–7, Table 3 lists sample simulation results to illustrate possible extent of the influence of phase function on modeled optical response of labeled tissues. In all cases, the reflectance values have been scaled such that the intensity for normal tissue equals one. The percentages included in parentheses reiterate the degree of overprediction by the respective phase function.

4 Discussion

The results presented in this study indicate that computational analysis of photon propagation through nanoparticle-labeled tissues requires a meticulous consideration of model input. The addition of nanoparticles can significantly alter the scattering and absorption coefficients as well as the anisotropy factor, but our results reveal that the exact form of the phase function used to model labeled tissues can also play an important role in determining the reflectance response. Further, it is evident that the extent of the influence of phase function is highly dependent on the optical sensor geometry simulated.

When the fibers are oriented perpendicular to the tissue surface, the inherent diagnostic contrast is negative; most of the detected photons penetrate deep into the stroma and the drop in intensity with development of precancer is due to increased stromal absorption and reduced stromal scattering.[22,27] It has been previously shown that tilted fibers demonstrate preferential sensitivity to the top epithelial layer. In this case, the inherent diagnostic contrast is expected to be positive; detected photons are mostly confined to the epithelium and increased epithelial scattering associated with development of precancer gives rise to higher intensity values.[27,36] Even though the main motivation behind nanoparticle labeling is to enhance the inherent contrast for improved diagnosis, the results in Figs. 4–7 demonstrate that the interplay of coincident changes in epithelial scattering

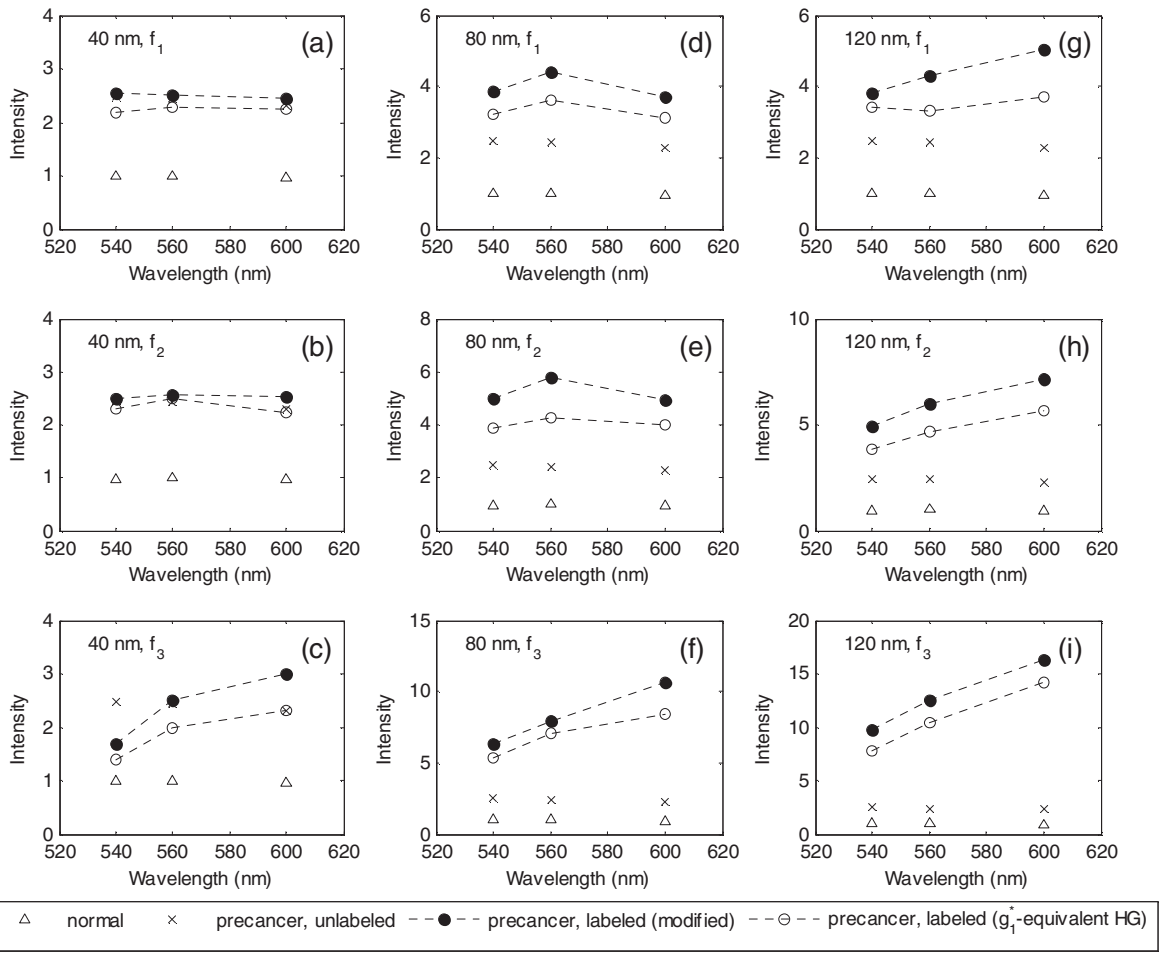

Fig. 6 Modeled reflectance response of normal tissue, unlabeled precancerous tissue, and precancerous tissue labeled with gold nanospheres. Possible combinations of nanosphere sizes (40, 80, and 120 nm) and volume fractions ($f_1 = 0.0005\%$, $f_2 = 0.001\%$, and $f_3 = 0.005\%$) result in nine different labeling schemes: (a) 40 nm; f_1, (b) 40 nm; f_2, (c) 40 nm; f_3, (d) 80 nm; f_1, (e) 80 nm; f_2, (f) 80 nm; f_3, (g) 120 nm; f_1, (h) 120 nm; f_2, and (i) 120 nm; f_3. The distal ends of the source and detector fibers are tilted toward each other and are separated by a center-to-center distance of 150 μm.

and absorption properties can lead to geometry-dependent contrast trends. For perpendicular fibers, a nanoparticle-induced increase in epithelial absorption may have a dominating influence on the reflectance profile causing a negative contrast enhancement. This is especially pertinent to 40- and 80-nm nanospheres, whereas the overall effect of labeling with 120-nm nanospheres is quite unpredictable. For tilted fibers, on the other hand, a nanoparticle-induced increase in epithelial scattering may have a dominating influence causing a positive contrast enhancement. Labeling schemes that employ 120-nm nanospheres exhibit this trend, but we note that the effect of adding 40- or 80-nm nanospheres is hard to predict since the observed contrast profile is also dependent on the source-detector separation considered.

Intensity variations arising from the use of different phase functions, however, are directly traceable to the results displayed in Figs. 1–3. Perpendicular fibers are particularly sensitive to near-forward ($<\sim$10 deg) and backward ($>\sim$160 deg) scattering events. For most labeling schemes, modified phase functions exceed their g_1^*-equivalent HG counterparts over these angular ranges. It appears that higher forward scattering probability predicted with modified phase functions is the dominant factor that affects the reflectance profile; photons are directed into deeper tissue regions giving way for more extensive absorption and, hence, the detected reflectance intensity is lower. With the corresponding HG functions, lower forward scattering probability suggests that detected photons tend to remain at more superficial tissue depths and, hence, MC results point to higher intensity levels. Differences in forward scattering probability are most pronounced for larger spheres added at the highest volume fraction considered and these translate into more significant changes in MC output.

It has been reported that fibers tilted at 30 deg demonstrate enhanced sensitivity to the phase function over the angular range $\sim$100 to 150 deg.[27] When the source and detector fibers are very close to each other, the majority of detected photons undergo a single intermediate-angle scattering event in the epithelium and the scattering angle falls into the specified range. For all of the labeling schemes tested, scattering probability over this angular range is higher for modified phase functions compared to their HG counterparts. Hence, it is not surprising at all that MC simulations carried out with modified phase functions predict higher intensity levels. If the source-detector separation is larger, photons may first experience near-forward

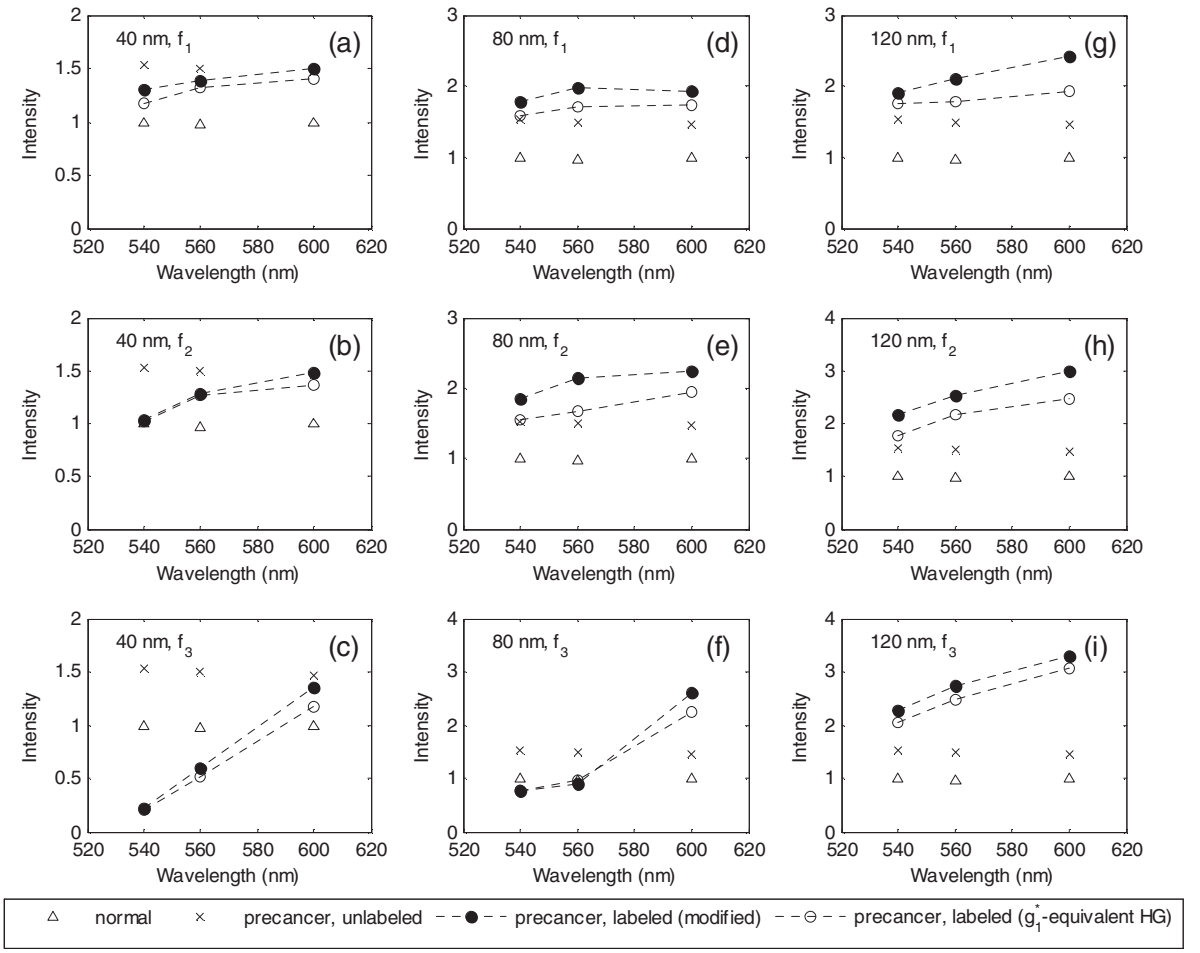

Fig. 7 Modeled reflectance response of normal tissue, unlabeled precancerous tissue, and precancerous tissue labeled with gold nanospheres. Possible combinations of nanosphere sizes (40, 80, and 120 nm) and volume fractions ($f_1 = 0.0005\%$, $f_2 = 0.001\%$, and $f_3 = 0.005\%$) result in nine different labeling schemes: (a) 40 nm; f_1, (b) 40 nm; f_2, (c) 40 nm; f_3, (d) 80 nm; f_1, (e) 80 nm; f_2, (f) 80 nm; f_3, (g) 120 nm; f_1, (h) 120 nm; f_2, and (i) 120 nm; f_3. The distal ends of the source and detector fibers are tilted toward each other and are separated by a center-to-center distance of 300 μm.

scattering before deflecting through ~100 to 150 deg toward the detector. In this case, higher forward scattering probability characterizing modified phase functions will increase the penetration depth making photons more prone to absorption. Depending on the labeling scheme considered, these competing factors may result in no observable difference in the reflectance intensity computed with modified and HG phase functions.

Overall, even though it is easier to compute the modified anisotropy factor and describe the angular scattering properties of labeled tissues with an analytical HG phase function, our results indicate that such an approximation may lead to incorrect and sometimes misleading model predictions regarding the expected contrast profile. We note, however, that MC modeling studies presented in this work employed a series of assumptions that merit discussion. First, labeling was specific to precancerous tissue and distribution of nanoparticles was uniform throughout the entire thickness of the epithelial layer. As indicated earlier, nanoparticles can be attached to molecules that have high affinity for cellular cancer biomarkers and various conjugation strategies have also been developed to reduce nonspecific labeling.[3–9,15,16,18] Uniform epithelial delivery, on the other hand, can be achieved through administration of permeation enhancers.[37] A common target in diagnostic studies is epidermal growth factor receptor (EGFR), which is overexpressed in epithelial precancers; significant labeling is observed when gold nanoparticles conjugated to anti-EGFR are added to precancerous tissue samples, whereas labeling is much less pronounced in normal samples.[6,38] In applications involving systemic delivery, passive extravasation from leaky vasculature aids in selective accumulation of nanoparticles in precancerous tissue.[9,35] For topical applications, some deposition of particles might inevitably occur in normal tissue, but there is currently no quantitative information and, hence, no indication as to whether any such unwanted deposition can alter the conclusions of this study. In modeling labeled precancerous tissue, we did not consider any potential influence of particle spacing and our calculations were based on the assumption of low volume fraction and, hence, independent scattering. It is known that interparticle effects become significant for center-to-center distances of less than about three times the particle radius.[18] When gold nanoparticles are conjugated to anti-EGFR, for instance, labeling predominantly occurs on the cell membrane.[6,38] This is the type of labeling strategy we envision and nanoparticle volume fractions we simulate are so low that a rough estimation for 10-μm cells points to a surface coverage of less than 5% in all cases. Under these conditions, it is highly unlikely that interparticle

Table 3 Sample simulation results to illustrate possible extent of the influence of phase function on modeled optical response of tissues labeled with gold nanospheres. The three different volume fractions indicated are: $f_1 = 0.0005\%$, $f_2 = 0.001\%$, and $f_3 = 0.005\%$. In all cases, the reflectance values have been scaled such that the intensity for normal tissue equals one. The percentages in parentheses specify the degree of overprediction by the respective phase function.

			Reflectance intensity relative to normal tissue		
Optical sensor geometry	Labeling scheme	λ (nm)	Precancer, unlabeled	Precancer, labeled (modified)	Precancer, labeled (g_1^*-equivalent HG)
Perpendicular fibers separated by 150 μm	80 nm; f_3	560	0.57	0.26	0.36 (~40%)
Perpendicular fibers separated by 150 μm	120 nm; f_3	600	0.63	0.88	1.19 (~35%)
Perpendicular fibers separated by 300 μm	80 nm; f_3	600	0.63	0.29	0.41 (~40%)
Perpendicular fibers separated by 300 μm	120 nm; f_3	540	0.56	0.28	0.40 (~40%)
Perpendicular fibers separated by 300 μm	120 nm; f_3	560	0.54	0.34	0.54 (~60%)
Perpendicular fibers separated by 300 μm	120 nm; f_3	600	0.63	0.47	0.76 (~60%)
Tilted fibers separated by 150 μm	80 nm; f_2	560	2.43	5.77 (~35%)	4.25
Tilted fibers separated by 150 μm	120 nm; f_1	600	2.40	5.22 (~35%)	3.86

effects will have any implications on the results presented here. Previous studies suggest that internalization of EGFR and the resulting biomarker-mediated aggregation of nanoparticles in small organelles can lead to a red shift in scattering maxima along with a considerable increase in scattering cross section per particle.[5,6,8,15,16,18,38] Aggregation effects are also evident when nanoparticles are targeted to intracellular biomarkers such as human papillomavirus related oncoproteins.[38] Details regarding specific aggregation patterns are largely unknown and our study does not address this issue. We can, however, hypothesize that the influence of phase function will be even more extensive in situations where particle aggregation causes increased scattering. Finally, we used nanospheres as labeling agents to demonstrate the importance of generating a proper form of phase function. Nanospheres are commonly encountered and yet simple to analyze, but similar conclusions are expected to apply to other types of nanoparticles such as nanorods and nanoshells with large optical cross sections that can significantly alter the angular scattering properties of tissues. As a side remark, metal nanoparticles can also generate contrast by creating field enhancement and exciting fluorescent markers.[5] Although this study focused on analyzing the reflectance profile of labeled tissues, it is possible to extend MC modeling and track fluorescence signals that would be detected in such a scenario.

5 Conclusions

The goal of the research described in this paper was to simulate photon propagation through nanoparticle-labeled epithelial tissues and to reveal the importance of using a proper form of scattering phase function for modeling purposes. As evidenced by the results presented, approximating phase functions may prove inadequate in predicting the extent of contrast enhancement due to labeling and may even alter the perceived contrast profile. It is also worth pointing out, once again, that the addition of nanoparticles gives rise to coincident changes in epithelial scattering and absorption properties, and whether these changes lead to an overall increase or decrease in detected reflectance intensity depends on the labeling scheme considered and the source-detector geometry simulated. Even though this study focused on investigating the reflectance response at a few representative wavelengths, a detailed assessment of the diagnostic potential of nanoparticle-enhanced measurements calls for an extended geometry-specific spectral analysis of optical signals obtained from labeled tissues.

References

1. N. Thekkek and R. Richards-Kortum, "Optical imaging for cervical cancer detection: solutions for a continuing global problem," *Nat. Rev. Cancer* **8**(9), 725–731 (2008).
2. J. Q. Brown, K. Vishwanath, G. M. Palmer, and N. Ramanujam, "Advances in quantitative UV-visible spectroscopy for clinical and preclinical application in cancer," *Curr. Opin. Biotechnol.* **20**(1), 119–131 (2009).
3. S. Kumar and R. Richards-Kortum, "Optical molecular imaging agents for cancer diagnostics and therapeutics," *Nanomedicine* **1**(1), 23–30 (2006).
4. L. R. Hirsch, A. M. Gobin, A. R. Lowery, F. Tam, R. A. Drezek, N. J. Halas, and J. L. West, "Metal nanoshells," *Ann. Biomed. Eng.* **34**(1), 15–22 (2006).

5. A. Wax and K. Sokolov, "Molecular imaging and darkfield microspectroscopy of live cells using gold plasmonic nanoparticles," *Laser Photonics Rev.* **3**(1–2), 146–158 (2009).
6. K. Sokolov, M. Follen, J. Aaron, I. Pavlova, A. Malpica, R. Lotan, and R. Richards-Kortum, "Real-time vital optical imaging of precancer using anti-epidermal growth factor receptor antibodies conjugated to gold nanoparticles," *Cancer Res.* **63**(9), 1999–2004 (2003).
7. C. Loo, L. Hirsch, M. Lee, E. Chang, J. West, N. Halas, and R. Drezek, "Gold nanoshell bioconjugates for molecular imaging in living cells," *Opt. Lett.* **30**(9), 1012–1014 (2005).
8. I. H. El-Sayed, X. H. Huang, and M. A. El-Sayed, "Surface plasmon resonance scattering and absorption of anti-EGFR antibody conjugated gold nanoparticles in cancer diagnostics: applications in oral cancer," *Nano Lett.* **5**(5), 829–834 (2005).
9. A. M. Gobin, M. H. Lee, N. J. Halas, W. D. James, R. A. Drezek, and J. L. West, "Near-infrared resonant nanoshells for combined optical imaging and photothermal cancer therapy," *Nano Lett.* **7**(7), 1929–1934 (2007).
10. J. Yguerabide and E. E. Yguerabide, "Light-scattering submicroscopic particles as highly fluorescent analogs and their use as tracer labels in clinical and biological applications – I. Theory," *Anal. Biochem.* **262**(2), 137–156 (1998).
11. J. Yguerabide and E. E. Yguerabide, "Light-scattering submicroscopic particles as highly fluorescent analogs and their use as tracer labels in clinical and biological applications – II. Experimental characterization," *Anal. Biochem.* **262**(2), 157–176 (1998).
12. P. K. Jain, K. S. Lee, I. H. El-Sayed, and M. A. El-Sayed, "Calculated absorption and scattering properties of gold nanoparticles of different size, shape, and composition: applications in biological imaging and biomedicine," *J. Phys. Chem. B* **110**(14), 7238–7248 (2006).
13. B. Khlebtsov and N. Khlebtsov, "Ultrasharp light-scattering resonances of structured nanospheres: effects of size-dependent dielectric functions," *J. Biomed. Opt.* **11**(4), 044002 (2006).
14. J. A. Gordon and R. W. Ziolkowski, "Investigating functionalized active coated nanoparticles for use in nano-sensing applications," *Opt. Express* **15**(20), 12562–12582 (2007).
15. J. Aaron, N. Nitin, K. Travis, S. Kumar, T. Collier, S. Y. Park, M. José-Yacamán, L. Coghlan, M. Follen, R. Richards-Kortum, and K. Sokolov, "Plasmon resonance coupling of metal nanoparticles for molecular imaging of carcinogenesis *in vivo*," *J. Biomed. Opt.* **12**(3), 034007 (2007).
16. J. Aaron, E. de la Rosa, K. Travis, N. Harrison, J. Burt, M. José-Yacamán, and K. Sokolov, "Polarization microscopy with stellated gold nanoparticles for robust, *in-situ* monitoring of biomolecules," *Opt. Express* **16**(3), 2153–2167 (2008).
17. Y. Hu, R. C. Fleming, and R. Drezek, "Optical properties of gold-silica-gold multilayer nanoshells," *Opt. Express* **16**(24), 19579–19591 (2008).
18. J. Aaron, K. Travis, N. Harrison, and K. Sokolov, "Dynamic imaging of molecular assemblies in live cells based on nanoparticle plasmon resonance coupling," *Nano Lett.* **9**(10), 3612–3618 (2009).
19. N. Nitin, D. J. Javier, D. M. Roblyer, and R. Richards-Kortum, "Widefield and high-resolution reflectance imaging of gold and silver nanospheres," *J. Biomed. Opt.* **12**(5), 051505 (2007).
20. R. T. Zaman, P. Diagaradjane, J. C. Wang, J. Schwartz, N. Rajaram, K. L. Gill-Sharp, S. H. Cho, H. G. Rylander, III, J. D. Payne, S. Krishnan, and J. W. Tunnell, "*In vivo* detection of gold nanoshells in tumors using diffuse optical spectroscopy," *IEEE J. Sel. Top. Quantum Electron.* **13**(6), 1715–1720 (2007).
21. D. Hidović-Rowe and E. Claridge, "Modelling and validation of spectral reflectance for the colon," *Phys. Med. Biol.* **50**(6), 1071–1093 (2005).
22. D. Arifler, C. MacAulay, M. Follen, and R. Richards-Kortum, "Spatially resolved reflectance spectroscopy for diagnosis of cervical precancer: Monte Carlo modeling and comparison to clinical measurements," *J. Biomed. Opt.* **11**(6), 064027 (2006).
23. C. Zhu, G. M. Palmer, T. M. Breslin, J. Harter, and N. Ramanujam, "Diagnosis of breast cancer using fluorescence and diffuse reflectance spectroscopy: a Monte-Carlo-model-based approach," *J. Biomed.Opt.* **13**(3), 034015 (2008).
24. C. R. Weber, R. A. Schwarz, E. N. Atkinson, D. D. Cox, C. MacAulay, M. Follen, and R. Richards-Kortum, "Model-based analysis of reflectance and fluorescence spectra for *in vivo* detection of cervical dysplasia and cancer," *J. Biomed Opt.* **13**(6), 064016 (2008).
25. A. W. H. Lin, N. A. Lewinski, J. L. West, N. J. Halas, and R. A. Drezek, "Optically tunable nanoparticle contrast agents for early cancer detection: model-based analysis of gold nanoshells," *J. Biomed. Opt.* **10**(6), 064035 (2005).
26. J. R. Mourant, J. P. Freyer, A. H. Hielscher, A. A. Eick, D. Shen, and T. M. Johnson, "Mechanisms of light scattering from biological cells relevant to noninvasive optical-tissue diagnostics," *Appl. Opt.* **37**(16), 3586–3593 (1998).
27. C. Kortun, Y. R. Hijazi, and D. Arifler, "Combined Monte Carlo and finite-difference time-domain modeling for biophotonic analysis: implications on reflectance-based diagnosis of epithelial precancer," *J. Biomed. Opt.* **13**(3), 034014 (2008).
28. M. Kirillin, M. Shirmanova, M. Sirotkina, M. Bugrova, B. Khlebtsov, and E. Zagaynova, "Contrasting properties of gold nanoshells and titanium dioxide nanoparticles for optical coherence tomography imaging of skin: Monte Carlo simulation and *in vivo* study," *J. Biomed. Opt.* **14**(2), 021017 (2009).
29. L. Wang, S. L. Jacques, and L. Zheng, "MCML – Monte Carlo modeling of light transport in multi-layered tissues," *Comput. Methods Programs Biomed.* **47**(2), 131–146 (1995).
30. P. B. Johnson and R. W. Christy, "Optical constants of the noble metals," *Phys. Rev. B* **6**(12), 4370–4379 (1972).
31. R. D. Averitt, D. Sarkar, and N. J. Halas, "Plasmon resonance shifts of Au-coated Au_2S nanoshells: insight into multicomponent nanoparticle growth," *Phys. Rev. Lett.* **78**(22), 4217–4220 (1997).
32. S. Link and M. A. El-Sayed, "Spectral properties and relaxation dynamics of surface plasmon electronic oscillations in gold and silver nanodots and nanorods," *J. Phys. Chem. B* **103**(40), 8410–8426 (1999).
33. S. Berciaud, L. Cognet, P. Tamarat, and B. Lounis, "Observation of intrinsic size effects in the optical response of individual gold nanoparticles," *Nano Lett.* **5**(3), 515–518 (2005).
34. H. C. van de Hulst, *Light Scattering by Small Particles*, Dover, New York (1981).
35. A. Agrawal, S. Huang, A. W. H. Lin, M. Lee, J. K. Barton, R. A. Drezek, and T. J. Pfefer, "Quantitative evaluation of optical coherence tomography signal enhancement with gold nanoshells," *J. Biomed. Opt.* **11**(4), 041121 (2006).
36. D. Arifler, R. A. Schwarz, S. K. Chang, and R. Richards-Kortum, "Reflectance spectroscopy for diagnosis of epithelial precancer: model-based analysis of fiber-optic probe designs to resolve spectral information from epithelium and stroma," *Appl. Opt.* **44**(20), 4291–4305 (2005).
37. A. L. van de Ven, K. Adler-Storthz, and R. Richards-Kortum, "Delivery of optical contrast agents using Triton-X100, part 2: enhanced mucosal permeation for the detection of cancer biomarkers," *J. Biomed. Opt.* **14**(2), 021013 (2009).
38. K. Sokolov, J. Aaron, B. Hsu, D. Nida, A. Gillenwater, M. Follen, C. MacAulay, K. Adler-Storthz, B. Korgel, M. Descour, R. Pasqualini, W. Arap, W. Lam, and R. Richards-Kortum, "Optical systems for *in vivo* molecular imaging of cancer," *Technol. Cancer Res. Treat.* **2**(6), 491–504 (2003).